Nanoscale Horizons

ROYAL SOCIETY OF CHEMISTRY

COMMUNICATION

View Article Online
View Journal | View Issue

Cite this: *Nanoscale Horiz.*, 2024, 9, 1190

Received 8th February 2024,
Accepted 7th May 2024

DOI: 10.1039/d4nh00060a

rsc.li/nanoscale-horizons

White light powered antimicrobial nanoagents for triple photothermal, chemodynamic and photodynamic based sterilization†

Hua Tian,‡[ac] Houjuan Zhu,‡*[b] Yuling Xue,[a] Maonan Wang,[d] Kuoran Xing,[a] Zibiao Li,[b] Xian Jun Loh,[b] Enyi Ye,[b] Xianguang Ding,[e] Bang Lin Li,[f] Xueqiong Yin*[c] and David Tai Leong*[a]

Antibacterial nanoagents have been increasingly developed due to their favorable biocompatibility, cost-effective raw materials, and alternative chemical or optical properties. Nevertheless, there is still a pressing need for antibacterial nanoagents that exhibit outstanding bacteria-binding capabilities and high antibacterial efficiency. In this study, we constructed a multifunctional cascade bioreactor (GCDCO) as a novel antibacterial agent. This involved incorporating carbon dots (CDs), cobalt sulfide quantum dots (CoS_x QDs), and glucose oxidase (GOx) to enhance bacterial inhibition under sunlight irradiation. The GCDCO demonstrated highly efficient antibacterial capabilities attributed to its favorable photothermal properties, photodynamic activity, as well as the synergistic effects of hyperthermia, glucose-augmented chemodynamic action, and additional photodynamic activity. Within this cascade bioreactor, CDs played the role of a photosensitizer for photodynamic therapy (PDT), capable of generating $^{\bullet}O_2^-$ even under solar light irradiation. The CoS_x QDs not only functioned as a catalytic component to decompose hydrogen peroxide (H_2O_2) and generate hydroxyl radicals (•OH), but they also served as heat generators to enhance the Fenton-like catalysis process. Furthermore, GOx was incorporated into this cascade bioreactor to internally supply H_2O_2 by consuming glucose for a Fenton-like reaction. As a result, GCDCO could generate a substantial amount of reactive oxygen species (ROS), leading to a significant synergistic effect that greatly induced bacterial death. Furthermore, the *in vitro* antibacterial experiment revealed that GCDCO displayed notably enhanced antibacterial activity against *E. coli* (99+ %) when combined with glucose under simulated sunlight, surpassing the efficacy of the individual components. This underscores its remarkable efficiency in combating bacterial growth. Taken together, our GCDCO demonstrates significant potential for use in the routine treatment of skin infections among diabetic patients.

New concepts

Antibiotic bacterial resistance is a major issue for infectious disease healthcare. As resistance arises usually through the repeated and chronic use of the same antibacterial modality, we try to confuse the otherwise responsive evolutionary machinery of bacteria by incorporating triple modalities of causing damage to the bacterial protective cell wall and later damage to their bacterial cytoplasms. These three concurrent onslaughts on the bacteria of photothermal, chemodynamic and photodynamic damages are produced using defect-engineered cobalt sulfide, carbon dots and glucose oxidase package in one system. The speed of production of the photothermal and photodynamic modalities upon activation with white light is instantaneous and can catch the bacteria off-guard. The design of white light excitation is intentional as white light can simply be driven by sunlight, which does not necessitate the use of lasers that tend to be hard in typical healthcare facilities giving flexibility to the patients and the laser-point sources may not be that suitable for large coverage wounds. We showed that indeed triple modality with focus on fast killing coupled with multiple modalities can greatly demonopolize the dominance of antibiotic use in treating infected wounds.

[a] *Department of Chemical and Biomolecular Engineering, National University of Singapore, Singapore 117585, Singapore. E-mail: cheltwd@nus.edu.sg*
[b] *Institute of Materials Research and Engineering (IMRE), Agency for Science, Technology and Research (A*STAR), 2 Fusionopolis Way, Innovis #08-03, Singapore 138634, Singapore. E-mail: zhu_houjuan@imre.a-star.edu.sg*
[c] *Hainan Provincial Fine Chemical Engineering Research Centre, Hainan University, Haikou, Hainan, 570228, P. R. China. E-mail: yxq88@hotmail.com*
[d] *Department of Pathology, Xiangya Hospital, School of Basic Medical Sciences, Central South University, Changsha, China*
[e] *Key Laboratory for Organic Electronics and Information Displays & Jiangsu Key Laboratory for Biosensors, Nanjing University of Posts & Telecommunications, Nanjing, 210023, China*
[f] *School of Chemistry and Chemical Engineering, Southwest University, Chongqing 400715, P. R. China*

† Electronic supplementary information (ESI) available. See DOI: https://doi.org/10.1039/d4nh00060a

‡ All these authors contributed equally.

1. Introduction

Individuals with diabetes mellitus, while not necessarily experiencing low survivability, often endure a deteriorating progression in their quality of life. Notably, these patients face an increased susceptibility to various complications, including skin and soft tissue infections such as cellulitis, osteomyelitis, and postoperative wound infections. The heightened risk is attributed to end-organ damage resulting from elevated blood sugar levels. Infected wounds, particularly those affecting the feet, are prevalent among individuals with diabetes, underscoring the challenges associated with managing and treating these complications.[1–5] Traditionally, antibiotics have been the predominant approach for treating wound infections. However, the prolonged and widespread use of antibiotics has led to an emerging concern – bacterial resistance to these drugs. The overreliance on antibiotics contributes to the development of resistant strains, making it increasingly challenging to effectively combat bacterial infections using conventional antibiotic therapies.[6] Currently, non-antibiotic treatments like near-infrared (NIR) activated photodynamic therapy (PDT) and photothermal therapy (PTT) have gained significant attention in research.[7–9] However, these methods pose challenges as they often demand a substantial mass of samples and the use of specialized optical equipment.[10,11] Moreover, the implementation of these photo-energized treatments requires specialized training to ensure safe and proficient application. The pandemic has underscored deficiencies in medical resources, particularly for conditions necessitating consistent and regular hospitalization attention. In response to these challenges, our objective is to achieve comparable treatment outcomes without relying on sophisticated hospital resources. This approach aims to enhance accessibility and address the limitations posed by the need for extensive medical facilities, especially, during times of heightened strain on healthcare systems. This motivation propelled us to develop a pragmatic strategy that eliminates the requirement for hospital equipment to achieve photo-driven antimicrobial effects. Our approach aims to bypass the necessity for photoexcitation sources located within hospitals, providing a more accessible and versatile solution for the implementation of photo-driven therapies. Hence, our focus centered on harnessing normal sunlight as a photoexcitation source. Although the luminosity of regular white light and sunlight may be lower compared to a laser with a well-defined spectrum, a key advantage lies in the broader area of illumination that sunlight provides. This advantage becomes particularly noteworthy, as the illuminated area from sunlight is significantly larger than that of a single medical laser light source. As clinical wounds typically exceed the size of a pin-sized laser point, the utilization of normal sunlight emerges as a practical, non-hospital-based strategy. However, we acknowledge the variability in solar power, which may not be consistent and standardized across all times of the day, seasons, and global locations. To enhance the reliability of action under diverse working conditions, we recognized the need to incorporate additional antimicrobial modalities.

Herein, we employed sunlight spectral activated carbon dots (CDs)[12–17] and cobalt sulfide quantum dots (CoS_x QDs) to generate a potent combination of photodynamic oxidative stress and chemodynamic therapy (CDT) for antimicrobial purposes in wound management.[18] Chemodynamic therapy (CDT) constitutes a novel treatment approach relying on Fenton or Fenton-like reactions. Diverse metal-based Fenton reagents, such as cobalt (Co), copper (Cu), molybdenum (Mo), and others, have been formulated to catalyze the conversion of intracellular hydrogen peroxide (H_2O_2) into highly reactive hydroxyl radicals ($^{\bullet}OH$) for CDT. This process disrupts the equilibrium of intracellular redox/oxidation states, leading to damage to cell organelles.[19–22] The effectiveness of CDT heavily relies on H_2O_2 as a crucial component. However, the limited availability of H_2O_2 in the wound microenvironment significantly hampers the efficiency of CDT.[23] Consequently, there is an urgent need to devise effective methods to overcome these limitations in CDT-based therapeutic applications.

Glucose oxidase (GOx) emerges as a promising oxidoreductase in this context, as it facilitates the conversion of glucose and oxygen into gluconic acid and H_2O_2. This enzymatic process has garnered significant research interest due to its potential to enhance the chemodynamic (CD) effect.[24] Indeed, diabetic patients exhibit elevated native blood glucose concentrations. The introduction of GOx into this context allows the enzymatic conversion of high blood glucose levels, generating H_2O_2. This enzymatic reaction proves advantageous in enhancing the efficiency of both CDT and PDT. Furthermore, PTT exploits photothermal nanoagents to convert light into heat, a mechanism that boosts CDT efficiency. This is achieved by elevating the local temperature, accelerating both the Fenton-like reaction and the enzymatic catalytic reaction of GOx. The synergy between PTT and CDT holds promise for enhanced therapeutic outcome.[25] CoS_x QDs, characterized as transition metal dichalcogenides (TMDs),[26–29] have been identified as Fenton-related CDT therapeutic agents according to previous reports.[30] Additionally, these CoS_x QDs not only demonstrate commendable photothermal performance but also exhibit a notable degree of photocatalytic effect. This multifunctional nature further enhances their therapeutic potential in the context of combined PTT and CDT. However, due to constraints imposed by the wound microenvironment, the combined photocatalytic and chemodynamic effects of CoS_x QDs may not generate a sufficient amount of reactive oxygen species (ROS) to effectively eliminate bacteria under sunlight irradiation. Therefore, to bolster the antibacterial efficacy of CoS_x QDs, it becomes imperative to devise antibacterial agents associated with CoS_x QDs.

In this study, we aimed to enhance the efficiency of bacterial infection treatment by employing a synergistic approach involving PDT, CDT, and PTT. To achieve this, we designed and developed a multifunctional cascade bioreactor termed GCDCO. This innovative antibacterial platform incorporated CDs, CoS_x QDs, and GOx for synergistic bacterial inactivation, as illustrated in Fig. 1. In the GCDCO system, CoS_x QDs played a crucial role as TMD QDs, exhibiting an outstanding photothermal (PT) effect

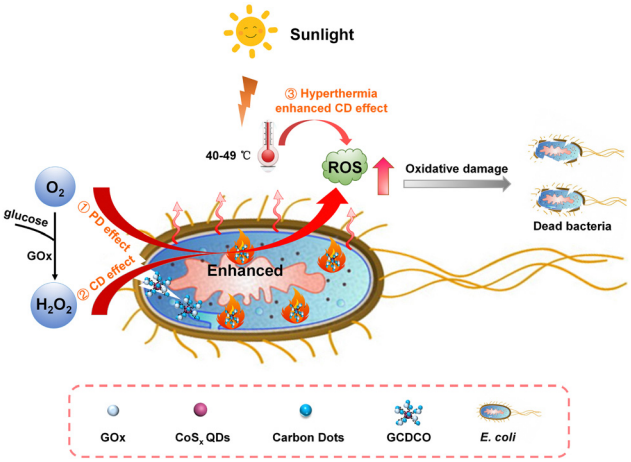

Fig. 1 Schematic illustration of cascade bioreactor GCDCO for achieving the hyperthermia-enhanced CD/PD effect and GOx-catalysis-enhanced CD effect of bacterial inactivation.

when exposed to sunlight. This PT effect not only contributed to the promotion of the chemodynamic (CD) effect, but also synergistically enhanced the overall therapeutic efficacy.[12–17] Carbon dots (CDs) served as photosensitizers, primarily employed to augment the photodynamic (PD) effect within the system. Concurrently, GOx functioned to convert glucose into H_2O_2, thereby intensifying the Fenton-like reaction. This capability allowed GOx to modulate the reaction environment, thereby further enhancing both CDT and PDT within the cascade bioreactor. In this study, we investigated the synergistic photothermal/chemodynamic/photodynamic (PT/CD/PD) performance of the GCDCO system. Additionally, we examined the facilitative effect of hyperthermia induced by PTT and H_2O_2 generated from GOx, which enhanced the CDs' photodynamic process. The cascade reactions collectively contributed to a significant enhancement in the antibacterial activity of GCDCO, particularly under simulated sunlight conditions. The promising results suggested that GCDCO holds substantial application potential for the treatment of secondary wound infections for diabetic patients.

2. Experimental

2.1 Materials

All chemicals and reagents (analytical grade) were used as received without any further purification. Cobalt chloride ($CoCl_2 \cdot 6H_2O$), sodium sulfide ($Na_2S \cdot 9H_2O$), bovine serum album (BSA), glucose oxidase (GOx), two kinds of 3,3′-diaminobenzidine tetrahydrochloride tablets (DAB and H_2O_2) and 2,7-dichlorofluorescin diacetate (DCF-DA) were purchased from Sigma-Aldrich Co., Ltd (USA). Methylene blue (MB), chitosan (CS, deacetylation degree ≥ 95%, Aladdin Ltd.) and ethylenediamine (EDA) were purchased from Marklin Chemical Co., Ltd (China). The lysogeny broth (LB) medium in all bacterial cultures was pre-treated by autoclaving at 120 °C for 20 min before use. Ultrapure water was obtained from a Milli-Q system (Health Force Biomeditech Holdings Ltd.).

2.2 Characterization

TEM images were obtained using a JEM 2100F transmission electron microscope under an acceleration voltage of 200 kV. UV-vis absorption spectra were obtained by using a Perkin-Elmer UV-vis spectrophotometer. The composition and structure of the sample were characterized by X-ray photoelectron spectroscopy (XPS; Kratos AXIS Ultra). The powder XRD measurements were performed using a Bruker D8 advanced diffractometer with Cu Kα irradiation in the 2θ range from 10° to 80°. The zeta potential and particle size were obtained by dynamic light scattering at room temperature using a Zetasizer Nano ZS (Malvern Instruments, UK). Scanning electron microscopy (SEM) images were obtained by using a field emission SEM (JEOL, JSM-7610FPlus) instrument. A PLS-SXE300 (200–2500 nm, 2335 W cm^{-2}) instrument purchased from PerfectLight Co., Ltd. was used for PT experiments. Cold light (400–800 nm, L-150 A) was used for PD experiments. Fluorescence emission and UV-vis spectra were recorded using a multimode reader (SynergyH4, Bio Tek).

2.3 Synthesis of cobalt sulphide quantum dots (CoS_x QDs)

In a typical procedure, the Co-precursor solution was firstly prepared by dispersing 0.5 mL $CoCl_2 \cdot 6H_2O$ solution (0.1 M) and 40 mg BSA in 40 mL water, and the pH value was adjusted to 3.0 by using 1 M HCl. Then, 0.2 mL $Na_2S \cdot 9H_2O$ (0.5 M) was dropped slowly under vigorous stirring at room temperature. After adjusting the pH value to neutral, a clear black solution of CoS_x QDs was produced quickly. Then the obtained black solution was purified by centrifugation (6000 rpm, 20 min) using an ultrafiltration centrifuge tube (MWCO 50 kDa) and centrifuged at 4 °C for several times. The concentration of CoS_x QDs was measured by ICP.

2.4 Synthesis of carbon dots (CDs)

6 mL ethylenediamine and 0.4 g CS were added into a beaker, and stirred for 15 min, after which 4 mL of concentrated sulfuric acid was slowly added dropwise. After the reaction was cooled to room temperature, 20 mL of distilled water was added, and the mixture was centrifuged (8000 rpm, 20 min). The supernatant was subsequently, collected and precipitated with 250 mL ethyl alcohol during 12 h. The mixture was filtered, the filtrate was concentrated by rotary evaporation, and finally dried in an oven at 60 °C. The CDs (0.70 g) were dispersed in ultrapure water as stock solution (10 mg mL^{-1}) for further study.

2.5 Synthesis of GCDCO

1 mL of CD solution (400 μg mL^{-1}), 1 mL of CoS_x QDs solution (800 μg mL^{-1}), and 1 mL of GOx solution (400 μg mL^{-1}) were mixed. Then, the mixture was kept at 4 °C for 8 h. The obtained GCDCO solution was filtered (0.22 μm) prior to storage.

2.6 Photothermal performance

The solution temperature was monitored by using an FLIR C2 thermal camera. Experiments were carried out in 0.2 mL of

different concentrations of CoS_x QDs solution (0, 25, 50, 100, 150, and 200 μg mL^{-1}) and GCDCO solution (containing different concentrations of 0, 16.67, 33.33, 66.67, and 133.33 μg mL^{-1} CoS_x QDs) under a sunlight intensity of 2335 W m^{-2} (2 sun).

2.7 Chemodynamic performance

DAB and MB were used to evaluate the amount of •OH generated by the Fenton-like reaction. Firstly, the amount of •OH was assessed in the presence of H_2O_2. For the DAB oxidation, 150 μL PBS (pH 4.6), 150 μL DAB solution, 50 μL samples and 50 μL H_2O_2 solution (200 mM) were mixed at 20 °C. The absorbance of DAB at 570 nm was measured. For the MB oxidation, 100 μL $NaHCO_3$ solution (100 mM), 50 μL MB solution (100 μg mL^{-1}), 50 μL samples and 100 μL H_2O_2 solution (50 mM) were mixed at 20 °C. The absorbance of MB at 660 nm was measured. Then, the amount of •OH was assessed in the presence of glucose without H_2O_2. For the DAB oxidation, 150 μL PBS (pH 4.6), 150 μL DAB solution, 50 μL samples and 100 μL glucose solution (6.4 mg mL^{-1}) were mixed at 20 °C. The absorbance of DAB at 570 nm was measured. For the MB oxidation, 100 μL $NaHCO_3$ solution (100 mM), 50 μL MB solution (100 μg mL^{-1}), 50 μL samples and 100 μL glucose solution (6.4 mg mL^{-1}) were mixed at 20 °C. The absorbance of MB at 660 nm was measured.

2.8 Thermally enhanced chemodynamic performance

The experimental steps are the same as in chemodynamic performance, and the experimental temperatures are controlled at 20, 37, 45, and 55 °C, respectively.

2.9 Photodynamic performance

The ROS was detected by 2,7-dichlorofluorescin diacetate (DCF-DA) with or without cold light (91 mW m^{-2}). 100 μL samples and 100 μL DCF-DA (10 μM) were mixed. Then, the mixtures were incubated for 0, 1, 2, 3, 4, 5, 6, 7, 8, 9, and 10 min, respectively. The fluorescence images were recorded at an excitation wavelength of 485 nm. In the presence of glucose, the ROS was detected using DCF-DA with or without cold light (91 mW m^{-2}). 100 μL samples, 100 μL DCF-DA (10 μM), and 100 μL glucose solution (6.4 mg mL^{-1}) were mixed, then the mixtures were incubated for 0, 1, 2, 3, 4, 5, 6, 7, 8, 9, and 10 min, respectively. The fluorescence images were recorded at an excitation wavelength of 485 nm.

2.10 Antibacterial activity evaluations *in vitro*

The antibacterial ability of GCDCO was investigated by using *E. coli*. The antibacterial properties of the different samples were studied by agar plate colony counting. Briefly, 150 μL bacterial solution (1×10^7 CFU mL^{-1}), 50 μL glucose solution (3.2 mg mL^{-1}) were added into 50 μL CDs, CoS_x QDs and GCDCO solution in a 48 well-plate. The solution was incubated at 37 °C for 3 h and illuminated with/without simulated sunlight (2335 W m^{-2}) for 5 min. Then, the bacterial suspension was diluted 1000 times with PBS and then 20 μL suspension was taken out and plated on an LB agar plate to grow for 18 h at 37 °C. The bacterial suspension suspended in PBS was used as a control. The colonies were counted at 18 h. The morphological characterization of the inactivated bacteria was carried out by SEM. After the samples were illuminated with/without simulated sunlight (2335 W m^{-2}) for 5 min, the bacteria were collected by centrifugation (8000 rpm, 15 min) and fixed with 200 μL 2.5% glutaraldehyde overnight at 4 °C. The bacteria samples were then dehydrated gradually using 200 μL each of increasing ethanol gradient concentrations (30%, 50%, 70%, 80%, 85%, 90%, 95%, and 100% ethanol), dried at 37 °C, and gold-sputtered prior to SEM observation.

3. Results and discussion

3.1 Synthesis and characterizations

The GCDCO nanoagents were synthesized in an aqueous environment at 4 °C using a straightforward composited route, as depicted in Fig. 2a. This novel construct consisted of three essential components: CoS_x quantum dots (QDs), carbon dots (CDs), and glucose oxidase (GOx). The CoS_x QDs, possessing a broad absorbance spectrum, were utilized as both enzyme catalysts and heat generators, significantly enhancing the production of ROS. CDs and GOx played distinct yet complementary roles within the GCDCO nanoagents. While CDs functioned as photosensitizers, absorbing light to induce photodynamic reactions, GOx served as the supplier of H_2O_2. This collaborative interplay between CDs and GOx synergistically contributed to an enhanced generation of ROS, reinforcing the overall antibacterial

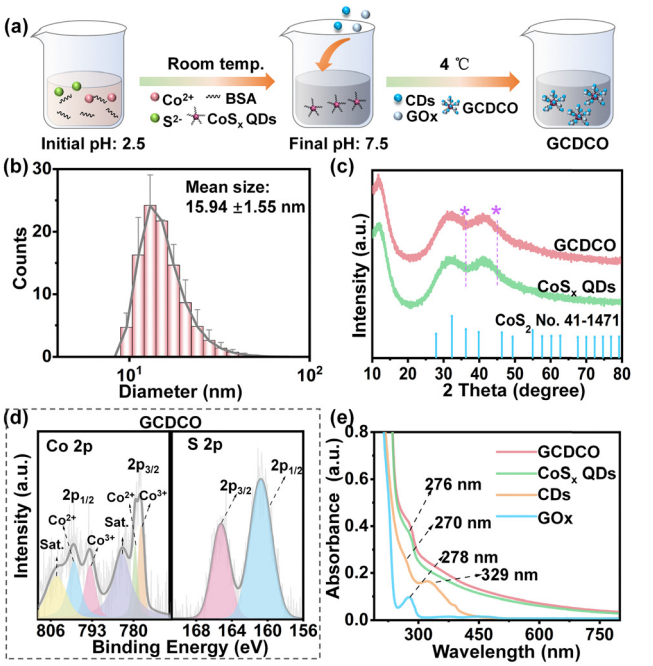

Fig. 2 Glucose oxidase-carbon dots-CoS_x QD (GCDCO) nanodevice characterization. (a) Synthesis schematic of GCDCO. (b) Particle size distribution of GCDCO. (c) XRD spectra, and (d) XPS spectra showing an unaffected structure of CoS_x QDs in GCDCO. (e) UV-vis absorption spectra of GCDCO, CoS_x QDs, CDs and GOx.

efficacy of the system. It was important to highlight that our system utilized white light or solar sunlight, eliminating the need for expensive equipment and mitigating the risk of eye burns associated with laser light. Furthermore, our research was conducted under mild conditions, avoiding the necessity for high pressure, elevated temperatures, or specialized apparatus and equipment. The resulting GCDCO solution exhibited a distinctive brownish color with excellent dispersibility. The transmission electron microscopy (TEM) images revealed that GCDCO, CoS_x QDs and CDs were all monodispersed and spherical (Fig. S1a, b, and c, ESI†). Specifically, the TEM images of GCDCO showcased the uniform dispersion of white GOx around CoS_x QDs and CDs. The hydrodynamic diameter of GCDCO was determined to be 15.94 ± 1.55 nm through dynamic light scattering (DLS), as depicted in Fig. 2b. This size was larger than that of CoS_x QDs, measuring 7.61 ± 0.32 nm (Fig. S1d, ESI†), providing further evidence of the composition of CoS_x QDs, CDs, and GOx in the GCDCO structure. Additionally, the surface charge of GCDCO was investigated by measuring its zeta potential, resulting in a value of −13.74 ± 1.59 mV. In comparison, the zeta potentials for individual components were determined as follows: −17.12 ± 0.51 mV for CoS_x QDs, −4.12 ± 0.95 mV for CDs, and −21.00 ± 2.21 mV for GOx. These zeta potential values provided insights into the electrostatic properties of each component, highlighting the overall charge characteristics of the GCDCO nanoagents. The observed changes in nanoparticle size and zeta potential can be attributed to the interactions among CoS_x QDs, CDs and GOx. Collectively, these variations in size and zeta potential served as a confirmatory evidence for the successful formation of GCDCO. To further assess the crystalline structures of GCDCO, X-ray diffraction (XRD) analysis was conducted. As illustrated in Fig. 2c, XRD spectra of GCDCO and CoS_x QDs exhibited striking similarity. The broader diffraction peak spanning from 20° to 50° closely matched the standard data for CoS_x (No. 41-1471), confirming the presence of CoS_x in the GCDCO structure. The broad nature of the peak was indicative of the small particle size and low crystallinity of CoS_x QDs. X-ray photoelectron spectroscopy (XPS) was employed to partially confirm the structure of GCDCO. For comparison, the XRD pattern of CDs showed a single broad peak at 21.98°, which corresponded to the (002) plane of graphitic carbon of crystalline nature (Fig. S1e, ESI†). This was not found in XRD pattern of GCDCO due to the shielding of strong CoS_x QDs' intensity. The results of elemental analysis, as presented in Table S1 (ESI†), indicated that the ratios of Co to S in CoS_x QDs and GCDCO were 1 : 2.08 and 1 : 2.93, respectively. These elemental ratios provided additional evidence supporting the incorporation of CoS_x QDs within the GCDCO structure. These observations aligned with the XRD results, indicating that the primary phase in CoS_x QDs was CoS_2, while in GCDCO, the presence of GOx was evident. Specifically, Fig. 2d illustrated that the peaks near 778 eV in the Co 2p spectra of GCDCO corresponded to CoS_x QDs, further supporting the characterization of the composite structure.[31] The S 2p spectra of GCDCO aligned with the spectra of S 2p in the CoS_x phase. Combining the results of XRD and XPS, it can be affirmed that the preparation of GCDCO was successful, with CoS_x QDs identified as the predominant phase within the GCDCO structure. Upon integrating the three components into a single entity, GCDCO exhibited an absorbance spectrum characterized by a broadening absorption band extending from the visible to near-infrared range. Additionally, two small peaks emerged, indicating significant potential for photothermal applications under sunlight, as illustrated in Fig. 2e. The broad peak around 276 nm in the absorption spectrum could be attributed to the combination of specific peaks, including the peak at 276 nm from CoS_x QDs, the peak at 278 nm from GOx, and the peak at 270 nm from CDs. Additionally, another absorption peak at around 330 nm was primarily associated with the n → π* transition of C=O in CDs.[32] This further suggested the facile integration of the three components, allowing for the preservation of the biological activity and natural structure of each constituent without compromising their integrity.

3.2 Investigation of photothermal performance

The photothermal performances of GCDCO and CoS_x QDs were evaluated at a sunlight intensity of 2335 W cm^{-2} (Fig. 3 and Fig. S2, ESI†). As shown in Fig. 3a, at the GCDCO concentration of 133.33 μg mL^{-1}, the solution temperature could be raised from 25 °C to 50.5 °C (increased by 24.5 °C) after irradiation by sunlight for 7 min, while the temperature of water exhibited a smaller increase (about 9.2 °C). In the infrared thermal images of GCDCO (Fig. 3b), the temperatures of GCDCO solutions exhibited a time- and concentration-dependent increase. This observation underscored the significant potential of GCDCO for PTT applications under sunlight irradiation, without the need for any special equipment.[33] The temperature of CoS_x QD solution at a concentration of 200 μg mL^{-1} increased by 27.4 °C (Fig. S2a, ESI†). As shown in Fig. S2b (ESI†), CoS_x QDs exhibited

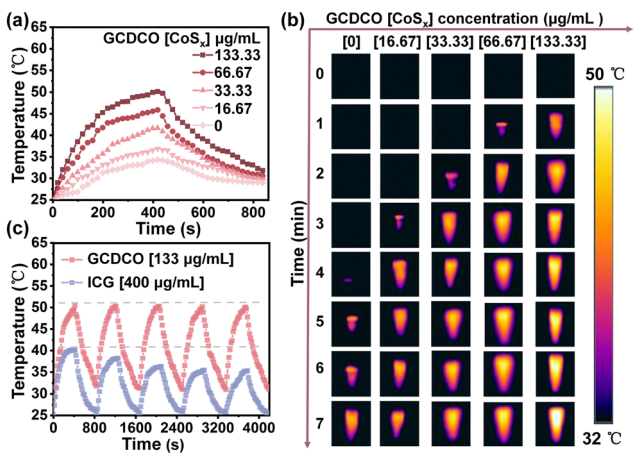

Fig. 3 Photothermal evaluation of GCDCO irradiated by simulated sunlight. (a) Photothermal heating curves of GCDCO solutions with various concentrations irradiated by simulated sunlight. (b) Infrared thermal images of GCDCO solutions at the indicated concentrations and irradiated for different durations. (c) Photothermal stability of GCDCO (133.33 μg mL^{-1}) and ICG (400 μg mL^{-1}) over 5 ON/OFF cycles of simulated sunlight irradiation (200–2500 nm, 2335 W cm^{-2}).

similar photothermal properties independently. By combining the photothermal analyses of GCDCO solutions and CoS_x QDs, we can conclude that the photothermal properties of CoS_x QDs were retained in GCDCO. This observation suggested that the presence of CDs and GOx did not significantly influence the inherent nature of CoS_x QDs. Simultaneously, the stability of GCDCO was thoroughly examined, with indocyanine green (ICG) employed as a control. ICG is a well-known commercial photothermal agent approved for clinical applications by the US Food and Drug Administration (FDA). In the course of 5 repeated irradiation cycles involving heating and cooling (Fig. 3c), the maximum temperatures of both GCDCO and CoS_x QDs (Fig. S2c, ESI†) remained relatively constant, in contrast to the gradual decrease observed in the maximum temperatures of ICG with increasing cycle numbers. This observation implied that the photothermal stability of GCDCO surpasses that of ICG. These findings suggested that, when compared to the commonly used commercial photothermal agent, GCDCO exhibited superior photothermal properties and stability.

3.3 Fenton-like properties of GCDCO

The outstanding Fenton-like activity of CoS_x QDs was attributed to the intrinsic multivalency of Co and defect engineering in the CoS_x QDs, as documented in previous studies.[30,34,35] To assess the Fenton-like reaction and H_2O_2 consumption mediated by GCDCO, we employed a cell-free system using 3,3′-diaminobenzidine tetrahydrochloride (DAB) as an indicator for •OH, as illustrated in Fig. 4a. In Fig. 4a1, a pronounced increase in A/A_0 (where A_0 represents the absorbance of DAB at 0 min and A is the absorbance of DAB at a given time) is evident, corresponding to the escalating concentration of GCDCO. Simultaneously, Fig. 4a2 depicts the reaction system with GCDCO ([CoS_x QDs] = 66.67 μg mL^{-1}), DAB, and H_2O_2. The absorption peak at 570 nm gradually intensified over time, and the color darkened (as evident in the inset picture) after 27 minutes. This observation indicated the oxidation of DAB, reflecting the production of •OH through the Fenton-like reaction. Additionally, the influence of H_2O_2 on various reaction systems was investigated. As shown in Fig. 4a3, both the GCDCO/DAB/H_2O_2 group and the CoS_x QDs/DAB/H_2O_2 group demonstrated significant Fenton-like activity, while other groups exhibited minimal response. Under identical conditions (Fig. S3a, ESI†), groups lacking H_2O_2 showed no production of ROS. It was evident that CoS_x QDs played a crucial role in GCDCO, attributed to the sulfur defect. Furthermore, the combination of CDs and GOx had minimal impact on the Fenton-like activity of CoS_x QDs when incorporated into the GCDCO structure.

Furthermore, to validate the reactive activation of the Fenton-like reaction, the degradation of methylene blue (MB) was investigated, as illustrated in Fig. 4b. In Fig. 4b1, a noticeable reduction in MB concentration was observed with an increasing concentration of GCDCO. The absorbance of MB at 660 nm exhibited a gradual decrease within approximately 30 min, signifying the rapid degradation of MB when GCDCO was introduced into the H_2O_2/MB system (Fig. 4b2). This observation underscored the contribution of GCDCO to the

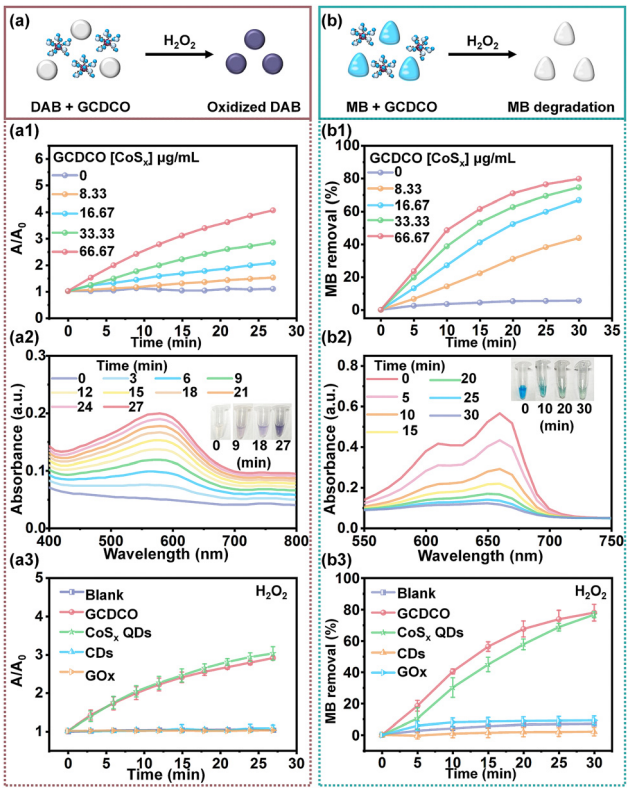

Fig. 4 Chemodynamic properties of GCDCO. (a) The evaluation of •OH production using probe DAB; (a1) A/A_0 with various concentrations of GCDCO at different times; (a2) UV spectra of reaction systems at different times, inset: solution color of DAB at 0, 9, 18, 27 minutes after incubation of GCDCO and 25 mM H_2O_2; and (a3) A/A_0 of different DAB reaction systems at different times with H_2O_2 (25 mM). (b) The evaluation of •OH production using probe MB; (b1) degradation of MB with various concentrations of GCDCO at different times; (b2) UV spectra of reaction systems at different times, inset: solution color of MB at 0, 10, 20, 30 minutes after incubation of GCDCO and 16.67 mM H_2O_2; and (b3) degradation of MB of different reaction systems with H_2O_2 (16.67 mM) at different times.

production of •OH. Furthermore, the influence of H_2O_2 on the system was also investigated. As demonstrated in Fig. S3b (ESI†), none of the samples exhibited MB degradation in the absence of H_2O_2. However, in the presence of H_2O_2, only GCDCO and CoS_x QDs demonstrated rapid MB degradation (Fig. 3b3). This observation underscored that the degradation of MB was indeed induced by the reaction between CoS_x QDs and H_2O_2. These results highlighted the exceptional Fenton-like activity of both GCDCO and CoS_x QDs, showcasing their promising potential in CDT against bacteria.

Furthermore, the presence of •OH generated in the presence of glucose without H_2O_2 was confirmed using DAB and MB (Fig. 5a). Upon adding GCDCO and CoS_x QDs into Glu/DAB, the absorption peak at 570 nm noticeably increased over time in the GCDCO/Glu/DAB group, while there was no significant change observed in the CoS_x QDs/Glu/DAB group. The value of A/A_0 was 2.56 in the GCDCO/Glu/DAB group, which was 2.5-times higher than that of the CoS_x QDs/Glu/DAB group (Fig. 5a1). In the MB degradation experiment, distinct degradation of the blue MB was observed in the GCDCO/Glu/MB group

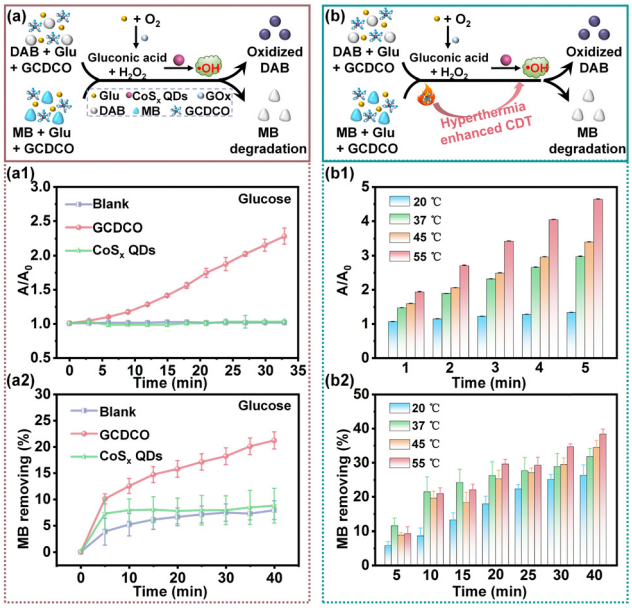

Fig. 5 The enhanced chemodynamic effect evaluation of GCDCO by GOx-catalysis. (a) GOx responsiveness promotes the production of •OH. The evaluation of •OH production using probes DAB and MB; (a1) time-dependent A/A_0 of different reaction systems by incubating with glucose; and (a2) time-dependent degradation of MB triggered by different reaction systems incubated with glucose. (b) Schematic illustration of hyperthermia enhanced CD effect; (b1) time-dependent A/A_0 changes by incubating with glucose under different temperatures; and (b2) time-dependent degradation of MB by incubating with glucose under different temperatures.

(Fig. 5a2), indicating the production of •OH resulting from the reaction between GOx and glucose. Upon incubation with GCDCO, more than 21% of MB experienced degradation, which was 2.4-times higher compared to the CoS_x QDs group. These findings suggested that GCDCO had the capability to initiate a Fenton-like reaction in the presence of glucose, without the addition of H_2O_2. This phenomenon arose from the oxidation reaction of glucose catalyzed by GOx, resulting in the generation of H_2O_2. Additionally, the impact of photothermal hyperthermia on the Fenton-like reaction was assessed using DAB and MB as indicators for •OH radicals (Fig. 5b). As depicted in Fig. 5b1, the A/A_0 at 55 °C was significantly higher than those recorded at 20 °C, 37 °C, and 45 °C, suggesting that an increase in temperature enhanced the production of •OH through the Fenton-like reaction. Additionally, the efficiency of MB degradation when incubated with glucose at 55 °C surpassed that of other groups (Fig. 5b2). The enhanced degradation at higher temperatures indicated that the elevation in temperature could augment the Fenton-like activity, contributing to a more efficient degradation process of MB. All these results collectively demonstrated that GOx played a beneficial role in a cascade reaction by supplying H_2O_2, thereby promoting the chemodynamic reaction to produce •OH. Additionally, photothermal hyperthermia was found to be another contributing factor responsible for enhancing •OH generation in the system.

3.4 Studies on ROS production ability

The confirmation of ROS generation was achieved through the use of the ROS probe 2,7-dichlorofluorescin diacetate (DCF-DA). This probe exhibited green emission upon oxidation, forming a fluorescent dye (DCF), as a result of interaction with •OH and $•O_2^-$. In the initial investigation, the generation of $•O_2^-$ was meticulously examined (Fig. 6a). As illustrated in Fig. 6a1, the ability to produce $•O_2^-$ was monitored and analysed using DCF-DA. The CoS_x QDs group exhibited a higher fluorescence intensity compared to the CDs group. This disparity could be attributed to the narrow band gap of CoS_x QDs, allowing for photocatalysis under visible light irradiation. Under visible light irradiation, CoS_x QDs entered an excited state, causing some electrons to transition from the valence band to the conduction band. Simultaneously, electron–hole pairs formed on the surface of CoS_x QDs. The electrons within CoS_x QDs had the ability to reduce molecular oxygen (O_2) in the aqueous solution, leading to a reaction with H_2O_2 and the production of $•O_2^-$.[36–38] CDs (carbon dots) have been previously reported as distinctive visible photosensitizers for the generation of $•O_2^-$, primarily attributed to energy transfer mechanisms.[39,40] Notably, the fluorescence enhancement (I/I_0) observed in the GCDCO group was the highest among all the groups studied. The data implied a synergistic effect between CoS_x QDs and CDs in enhancing $•O_2^-$ production. As depicted in Fig. 6a2, the $•O_2^-$ production exhibited a proportional relationship with the concentration of GCDCO. Furthermore,

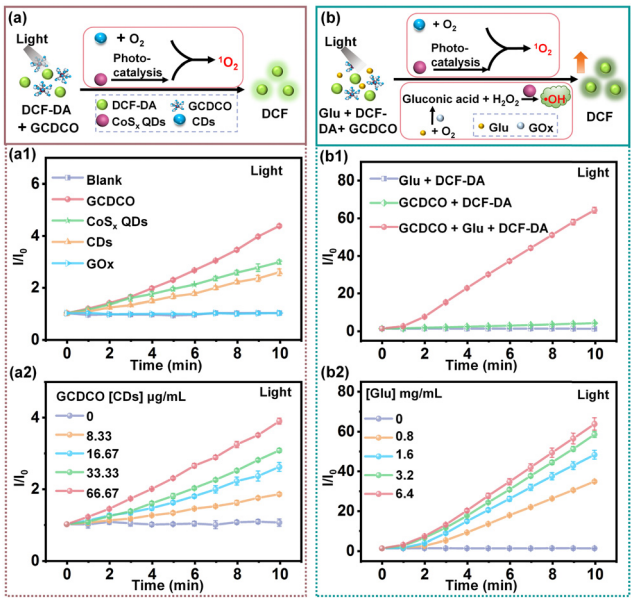

Fig. 6 ROS production from GCDCO under white light irradiation. (a) The evaluation of ROS production using probe DCF-DA in the absence of glucose; (a1) effect of light on the I/I_0 of different reaction systems at different times; and (a2) I/I_0 *versus* various concentrations of GCDCO at different times. (b) GOx responsiveness promotes the production of ROS. The evaluation of ROS production using probe DCF-DA in the presence of glucose; (b1) time-dependent fluorescence changes with cold-light irradiation (400–800 nm, 91 mW m^{-2}); and (b2) effect of glucose concentration on I/I_0 of GCDCO reaction system.

both the generation of $^{\bullet}OH$ in the chemodynamic process and the production of $^{\bullet}O_2^-$ in the photodynamic and photocatalysis processes were investigated and quantified using DCF-DA, as illustrated in Fig. 6b. The catalysis by GOx significantly enhanced the chemodynamic effect, resulting in the most prominent fluorescence enhancement (I/I_0) in the GCDCO/Glu/DCF-DA plus light group, as illustrated in Fig. 6b1. The I/I_0 values for various groups without light are presented in Fig. S4a (ESI†). Specifically, for the GCDCO/Glu/DCF-DA with light group, GCDCO/DCF-DA with light group, and GCDCO/Glu/DCF-DA without light group, the I/I_0 values were 42.90, 6.71, and 6.69, respectively. These results indicated that GCDCO exhibited a highly significant effect in the production of ROS under light irradiation. Furthermore, among various reaction systems, the GCDCO/Glu/DCF-DA with light group exhibited the highest enhanced fluorescence at 10 min, as illustrated in Fig. S4b (ESI†). This observation underscored the significant impact of GOx-catalysis in boosting the production of ROS under light irradiation. Additionally, the fluorescence enhancement of the GCDCO group increased with the rise in glucose concentration, as depicted in Fig. 6b2. Collectively, these findings suggested that the GCDCO/Glu/DCF-DA with light group had the capability to generate a higher amount of ROS, and the catalytic role of GOx promoted the cascade reaction, enhancing both CDT and PDT. This potential synergy exhibited promise for antibacterial therapy.

3.5 *In vitro* antibacterial efficacy

Building upon the aforementioned results, it was anticipated that GCDCO held the potential to eliminate bacteria through a synergistic effect, combining photothermal-enhanced CDT and GOx-catalysis-enhanced CDT/PDT. Prior to conducting antibacterial studies, we conducted preliminary *in vitro* investigations to evaluate the cytotoxicity of GCDCO *via* alamar blue assay. We treated separate groups of Immortalized human corneal epithelial cells (HCE) and LO2 cells with GCDCO at different concentrations. The cell viability of GCDCO gradually decreased to 16.2% and 15.6% as applied concentration increased to 53.33 μg mL^{-1}, which may be caused by the gluconic acid produced by GOx and the high concentration of H_2O_2 by-products (Fig. S5a and c, ESI†). To further validate the fact that the toxicity of GCDCO is originated from GOx, HCE cells treated with CDs, GOx and CoS_x QDs at three concentrations were chosen for comparison. Notably, only GOx exhibited high inhibition on cells, which was similar to that of our nanoagents (Fig. S5b, ESI†). Besides these, after incubating with CDs, GOx, CoS_x QDs and GCDCO dispersions at various concentrations for 6 h (but without glucose), it was observed that the LO2 cell viability of all groups remained at least 98% or higher even at high concentrations of 13.33 μg mL^{-1}, suggesting low intrinsic toxicity of all components (Fig. S5d, ESI†). These results verified the good cytocompatibility and the promising therapeutic property of our designed GCDCO nanoagents.

The antibacterial efficacy of GCDCO against *E. coli* was assessed through agar plate colony counting experiments. The minimum inhibitory concentration of GCDCO against

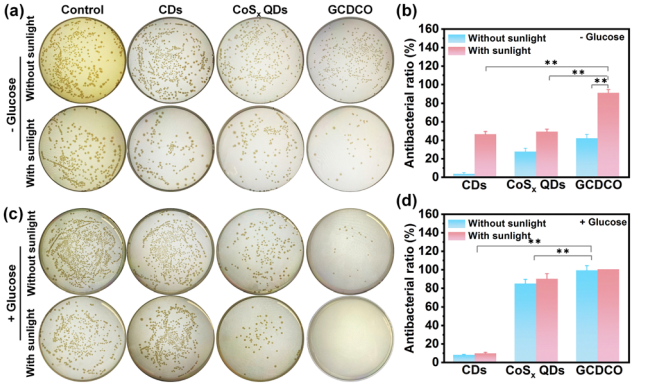

Fig. 7 Antibacterial characterization of *E. coli in vitro*. (a) Photographs of survived bacterial colonies of *E. coli* without sunlight and with sunlight treatment in the absence of glucose; (b) corresponding antibacterial activity of CDs (26.66 μg mL^{-1}), CoS_x QDs (53.33 μg mL^{-1}) and GCDCO (53.33 μg mL^{-1}); (c) photographs of survived bacterial colonies of *E. coli* without simulated sunlight (200–2500 nm, 2335 W cm^{-2}) and with simulated sunlight treatment in the presence of glucose; and (d) corresponding antibacterial activity of CDs, CoS_x QDs and GCDCO.

E. coli. was, respectively, determined to be 2.19 μg mL^{-1} for MIC50 and 4.04 μg mL^{-1} for MIC90 (Fig. S6, ESI†). Fig. 7a presents colony images of *E. coli* in the absence of glucose, while Fig. 7b illustrates the antibacterial activity of CDs, CoS_x QDs, and GCDCO, calculated based on the bacterial colony counts. In the GCDCO plus sunlight group, the antibacterial ratio was determined to be 90.63 ± 3.6%, surpassing the antibacterial activity observed for CDs and CoS_x QDs. Furthermore, the influence of glucose on the antibacterial activity of CoS_x QDs and GCDCO was investigated. Fig. 7c and d depict the results of antibacterial activity in the presence of glucose, with the GCDCO plus sunlight group exhibiting the highest antibacterial ratio (100%). The results indicated that GCDCO exhibited notable antibacterial activity compared to CDs and CoS_x QDs. Moreover, with the introduction of glucose, the catalytic activity of GOx significantly enhanced the eradication of *E. coli*. This suggested that the remarkable antibacterial activity of GCDCO was attributed to the synergistic effect and the cascade reaction, highlighting the potential for enhanced antibacterial efficacy. Additionally, the concentrations of CDs, GOx, CoS_x QDs and GCDCO were lowered to further investigate the synergistic antibacterial effect based on the bacterial colony counts and by calculating OD values of bacterial dispersions. To study the difference of CoS_x QDs and GCDCO in the presence of glucose, we firstly lowered down their concentration to 10 μg mL^{-1}. As shown in Fig. S7 (ESI†), the bacterial survival rates of GCDCO with and without sunlight irradiation were around 5.15% and 0.99%, which were, respectively, 18.44-times and 78.98-times lower than that for CoS_x QDs. However, not much difference in antibacterial activity between GCDCO and GOx was found at this concentration. The concentration of GCDCO lowered to 5 μg mL^{-1} was applied to investigate the antibacterial activity (Fig. S8, ESI†). We found that the bacterial survival rates of GCDCO with and without sunlight irradiation were 7.85-times and 4.53-times lower than that for CoS_x QDs,

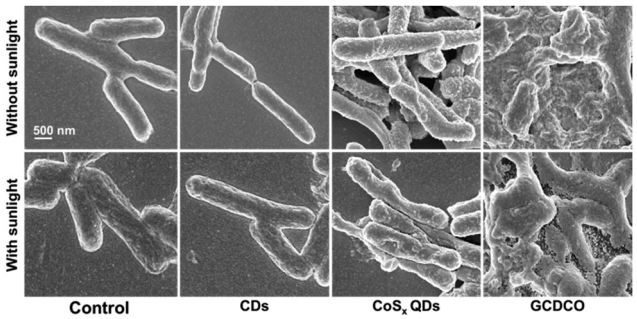

Fig. 8 SEM of GCDCO-, CoS_x QDs- and CDs-damaged *E. coli* cell walls with and without sunlight irradiation (200–2500 nm, 2335 W cm^{-2}).

as well as 2.93-times and 1.34-times lower than that for GOx. These antibacterial data all indicated the synergistic antibacterial activity of PTT and CD effects from CoS_x QDs, PDT effect from CDs, and glucose catalysed effect from GOx in GCDCO.

To provide further insight into the impact of GCDCO on bacterial morphology, the morphological changes of *E. coli* were observed using scanning electron microscopy (SEM) after treatment with lethal doses of GCDCO. As depicted in Fig. 8, the control group represented untreated *E. coli*, displaying intact cell walls with a smooth surface. After exposure to CoS_x QDs in the absence of sunlight, *E. coli* exhibited a roughened cell wall. When subjected to sunlight, *E. coli* treated with CoS_x QDs displayed partial surface collapse. In contrast, bacteria treated with GCDCO without sunlight experienced severe damage. Upon exposure to sunlight, the bacteria treated with GCDCO fully collapsed, leading to the leakage of cytoplasmic constituents. Eventually, the potent destructive impact of sunlight-activated GCDCO was manifested in the destruction of the cytoplasmic membrane through the synergistic enhancement of PTT and the catalysis-enhanced combination of CDT and PDT facilitated by GOx. This concerted approach ultimately resulted in the leakage of vital cytoplasmic content.

4. Conclusions

In summary, a versatile cascade bioreactor, GCDCO, designed for synergistic bacterial inactivation under sunlight, was successfully developed through a straightforward method. GCDCO demonstrated outstanding PTT effects in sunlight, enhancing CDT and showing photothermal synergistic enhancement of CDT. Additionally, the presence of GOx in GCDCO facilitated the catalysis of glucose, generating H_2O_2, which further decomposed into ROS through a Fenton-like reaction. This cascade reaction accelerated both CDT and PDT. Moreover, GCDCO exhibited significant antibacterial activity against *E. coli in vitro* (99+ %) in the presence of glucose, attributed to the GOx-catalysis-enhanced CDT and PDT, along with the photothermal synergistic enhancement of CDT. Consequently, this multifunctional cascade bioreactor holds promise as a reference for treating skin infections in diabetic patients under sunlight.

Author contributions

H. Tian performed the sensing investigations and analysed the data. H. J. Zhu performed the chemical, XRD, and electronic XPS studies, analysed the data, and drafted the manuscript with contributions from all authors. M. N. Wang, K. R. Xing, and Y. L. Xue repeated the experiments. X. G. Ding and B. L. Li reviewed the prepared figures. Z. B. Li, X. J. Loh, E. Y. Ye, X. Q. Yin, and D. T. Leong reviewed and edited the manuscript. All authors discussed the experimental results and commented on the manuscript.

Conflicts of interest

There are no conflicts to declare.

Acknowledgements

This work was supported by China Scholarship Council. We acknowledge the funding provided by the NUS Reimagine Grant (A-0009179-02-00; A-0009179-03-00).

Notes and references

1 M. Dryden, M. Baguneid, C. Eckmann, S. Corman, J. Stephens, C. Solem, J. Li, C. Charbonneau, N. Baillon-Plot and S. Haider, *Clin. Microbiol. Infect.*, 2015, **21**(Suppl 2), S27–S32.
2 C. Polk, M. M. Sampson, D. Roshdy and L. E. Davidson, *Infect. Dis. Clin. North Am.*, 2021, **35**, 183–197.
3 Q. Y. You, M. D. Hu and H. Qian, *Adv. Funct. Mater.*, 2024, 2315199.
4 H. Zhu, J. Mah Jian Qiang, C. G. Wang, C. Y. Chan, Q. Zhu, E. Ye, Z. Li and X. J. Loh, *Bioact. Mater.*, 2022, **18**, 471–491.
5 S. Wan, K. Wang, P. Huang, X. Guo, W. Liu, Y. Li, J. Zhang, Z. Li, J. Song, W. Yang, X. Zhang, X. Ding, D. T. Leong and L. Wang, *Nat. Commun.*, 2024, **15**, 3343.
6 M. A. Kohanski, D. J. Dwyer and J. J. Collins, *Nat. Rev. Microbiol.*, 2010, **8**, 423–435.
7 H. Zhu, Z. Li, E. Ye and D. T. Leong, *ACS Appl. Mater. Interfaces*, 2021, **13**, 60351–60361.
8 H. Zhu, J. Zheng, X. Y. Oh, C. Y. Chan, B. Q. L. Low, J. Q. Tor, W. Jiang, E. Ye, X. J. Loh and Z. Li, *ACS Nano*, 2023, **17**, 7953–7978.
9 H. Zhu, B. Li, C. Yu Chan, B. Low Qian Ling, J. Tor, X. Yi Oh, W. Jiang, E. Ye, Z. Li and X. Jun Loh, *Adv. Drug Delivery Rev.*, 2023, **192**, 114644.
10 Y. Yu, P. Li, C. Zhu, N. Ning, S. Zhang and G. J. Vancso, *Adv. Funct. Mater.*, 2019, **29**, 1904402.
11 Y. Yu, L. Mei, Y. Shi, X. Zhang, K. Cheng, F. Cao, L. Zhang, J. Xu, X. Li and Z. Xu, *J. Mater. Chem. B*, 2020, **8**, 1371–1382.
12 B. Geng, J. Hu, Y. Li, S. Feng, D. Pan, L. Feng and L. Shen, *Nat. Commun.*, 2022, **13**, 5735.

13 B. Geng, S. Xu, P. Li, X. Li, F. Fang, D. Pan and L. Shen, *Small*, 2022, **18**, 2103528.
14 B. Geng, W. Shen, F. Fang, H. Qin, P. Li, X. Wang, X. Li, D. Pan and L. Shen, *Carbon*, 2020, **162**, 220–233.
15 B. Geng, J. Hu, P. Li, D. Pan and L. Shen, *Carbon*, 2022, **187**, 365–374.
16 K. Jiang, S. Sun, L. Zhang, Y. Lu, A. Wu, C. Cai and H. Lin, *Angew. Chem., Int. Ed.*, 2015, **54**, 5360–5363.
17 N. Gong, X. Ma, X. Ye, Q. Zhou, X. Chen, X. Tan, S. Yao, S. Huo, T. Zhang, S. Chen, X. Teng, X. Hu, J. Yu, Y. Gan, H. Jiang, J. Li and X.-J. Liang, *Nat. Nanotechnol.*, 2019, **14**, 379–387.
18 P. Manivasagan, A. Joe, H. W. Han, T. Thambi, M. Selvaraj, K. Chidambaram, J. Kim and E. S. Jang, *Mater. Today Bio.*, 2022, **13**, 100197.
19 B. Ma, S. Wang, F. Liu, S. Zhang, J. Duan, Z. Li, Y. Kong, Y. Sang, H. Liu, W. Bu and L. Li, *J. Am. Chem. Soc.*, 2019, **141**, 849–857.
20 Y. Cheng, F. Yang, K. Zhang, Y. Zhang, Y. Cao, C. Liu, H. Lu, H. Dong and X. Zhang, *Adv. Funct. Mater.*, 2019, **29**, 1903850.
21 X. Liu, Z. Yan, Y. Zhang, Z. Liu, Y. Sun, J. Ren and X. Qu, *ACS Nano*, 2019, **13**, 5222–5230.
22 Y. Han, S. Gao, Y. Zhang, Q. Ni, Z. Li, X. J. Liang and J. Zhang, *Bioconjugate Chem.*, 2020, **31**, 1247–1258.
23 L. S. Lin, T. Huang, J. Song, X. Y. Ou, Z. Wang, H. Deng, R. Tian, Y. Liu, J. F. Wang, Y. Liu, G. Yu, Z. Zhou, S. Wang, G. Niu, H. H. Yang and X. Chen, *J. Am. Chem. Soc.*, 2019, **141**, 9937–9945.
24 L. H. Fu, C. Qi, J. Lin and P. Huang, *Chem. Soc. Rev.*, 2018, **47**, 6454–6472.
25 X. Liu, Y. Liu, J. Wang, T. Wei and Z. Dai, *ACS Appl. Mater. Interfaces*, 2019, **11**, 23065–23071.
26 B. L. Li, J. J. Luo, H. L. Zou, Q.-M. Zhang, L.-B. Zhao, H. Qian, H. Q. Luo, D. T. Leong and N. B. Li, *Nat. Commun.*, 2022, **13**, 7289.
27 H. Zhu, W. Zan, W. Chen, W. Jiang, X. Ding, B. L. Li, Y. Mu, L. Wang, S. Garaj and D. T. Leong, *Adv. Mater.*, 2022, **34**, e2200004.
28 H. Zhu, S. Huang, M. Ding, Z. Li, J. Li, S. Wang and D. T. Leong, *ACS Appl. Mater. Interfaces*, 2022, **14**, 25183–25196.
29 Y. Li, H. Tang, H. Zhu, A. Kakinen, D. Wang, N. Andrikopoulos, Y. Sun, A. Nandakumar, E. Kwak, T. P. Davis, D. T. Leong, F. Ding and P. C. Ke, *ACS Appl. Mater. Interfaces*, 2021, **13**, 29936–29948.
30 J. Ji, Q. Yan, P. Yin, S. Mine, M. Matsuoka and M. Xing, *Angew. Chem., Int. Ed.*, 2021, **60**, 2903–2908.
31 V. Singh, A. Tiwari and T. C. Nagaiah, *J. Mater. Chem. A*, 2018, **6**, 22545–22554.
32 Z. Guo, J. Luo, Z. Zhu, Z. Sun, X. Zhang, Z.-c Wu, F. Mo and A. Guan, *Dyes Pigm.*, 2020, **173**, 107952.
33 H. Zheng, S. Wang, L. Zhou, X. He, Z. Cheng, F. Cheng, Z. Liu, X. Wang, Y. Chen and Q. Zhang, *Chem. Eng. J.*, 2021, **404**, 126439.
34 J. Tian, H. Zhu, J. Chen, X. Zheng, H. Duan, K. Pu and P. Chen, *Small*, 2017, 13.
35 X. Ding, F. Peng, J. Zhou, W. Gong, G. Slaven, K. P. Loh, C. T. Lim and D. T. Leong, *Nat. Commun.*, 2019, **10**, 41.
36 J. Wang, Y. Wang, D. Zhang, C. Chen and Z. Yang, *ACS Appl. Nano Mater.*, 2021, **4**, 7698–7711.
37 Z.-D. Meng, L. Zhu, K. Ullah, S. Ye and W.-C. Oh, *Appl. Surf. Sci.*, 2013, **286**, 261–268.
38 Z.-D. Meng, L. Zhu, K. Ullah, S. Ye, Q. Sun, W. K. Jang and W.-C. Oh, *Mater. Res. Bull.*, 2014, **49**, 272–278.
39 Z. M. Markovic, M. Kovacova, P. Humpolicek, M. D. Budimir, J. Vajdak, P. Kubat, M. Micusik, H. Svajdlenkova, M. Danko, Z. Capakova, M. Lehocky, B. M. Todorovic Markovic and Z. Spitalsky, *Photodiagn. Photodyn. Ther.*, 2019, **26**, 342–349.
40 J. Ge, M. Lan, B. Zhou, W. Liu, L. Guo, H. Wang, Q. Jia, G. Niu, X. Huang, H. Zhou, X. Meng, P. Wang, C. S. Lee, W. Zhang and X. Han, *Nat. Commun.*, 2014, **5**, 4596.